The color ratio-intensity relation in the Jovian aurora: Hubble observations of auroral components

J.-C. Gérard, B. Bonfond, D. Grodent, A. Radioti

LPAP, Université de Liège, Belgium

To be published in Planetary and Space Science

June 2016

Abstract

Spectral observations made with the long slit of the Space Telescope Imaging Spectrograph (STIS) on board Hubble have been used to construct spectral maps of the FUV Jovian aurora. They reveal that the amount of absorption by overlying methane shows significant spatial variations. In this report, we examine the relationship between the auroral brightness of the unabsorbed H_2 emission that is proportional to the precipitated electron energy flux, and the ultraviolet color ratio, a proxy of the mean electron energy. We find that it varies significantly between the different components of the aurora and in the polar region. Although no global dependence can be found, we show that the two quantities are better organized in some auroral components such as regions of the main aurororal emission. By contrast, the dependence of the electron characteristic energy in high-latitude and diffuse aurora regions on the auroral energy input is generally more scattered. We conclude that the various auroral components are associated with different electron acceleration processes, some of which are not governed by a simple relation linking the value of a field-aligned acceleration potential with the parallel currents flowing from the ionosphere.

1. Introduction

The characteristic energy of the auroral electrons creating the Jovian aurora has not been measured in situ so far. Only two indirect methods have been used to remotely sense the penetration depth of auroral electrons. The first one consists in measuring the altitude of the emission peak of the aurora above the night planetary limb with an ultraviolet camera or spectrometer (Bonfond et al., 2009). Results based on this technique were recently reported by Bonfond et al., 2015) who analyzed FUV images of the north aurora obtained with the Space Telescope Imaging Spectrograph (STIS). Absorption signatures by hydrocarbons at the limb were clearly observed as a shift between the absorbed and unabsorbed brightness profiles. They found that the altitude of the brightness peak above the limb is close to 400 km, which is significantly higher than the ~250 km measured in visible wavelengths in the post-dusk sector (Vasavada et al., 1999). However, they could not draw a firm conclusion and suggested that the ultraviolet observations are not incompatible with an emission peak located at ~250 km.

The second approach is based on the characteristics of the emitted far ultraviolet auroral spectrum (Yung et al., 1982). Comparison between the observed UV spectrum and a reference H_2 laboratory spectrum is made to locate the bulk of the auroral emission relative to the hydrocarbon homopause. This approach uses the properties of the CH_4 absorption cross section in the ultraviolet. The methane molecules partly absorb the H_2 emissions at wavelengths below 140 nm while the longer wavelength H_2 emissions are not attenuated. If the mean energy of the electrons increases, the short wavelength part of the spectrum is more absorbed and the shape of the observed H_2 emission becomes significantly different from a reference (unabsorbed) laboratory or synthetic spectrum. Therefore, a FUV color ratio is

defined as

$$CR = I(155\text{-}162\ nm)/I(123\text{-}130\ nm), \quad (1)$$

where the nominator is the measured intensity (in photon units) integrated between 155 and 162 nm and the denominator is the total intensity between 123 and 130 nm. In the absence of hydrocarbon absorption, the value of the color ratio is ~1.1.

The FUV color ratio has been used to determine the characteristic energy of the auroral precipitation using spectra obtained from FUV spectrographs on board Earth-orbiting spacecraft such as the International Ultraviolet Explorer (IUE) (Livengood and Moos (1990), the Hopkins Ultraviolet Telescope (HUT) (Morrisey et al., 1997) and, mostly, the Hubble Space Telescope (HST). Visits during the Galileo orbiting mission have also provided global or local auroral color ratios (Ajello et al., 1998). A summary of these results was given by Clarke et al. (2004), Badman et al. (2014) and Gérard et al. (2014). Recently, Tao et al. (2015) defined an extreme ultraviolet (EUV) color ratio adapted to the jovian observations made with the EXCEED spectrometer on board the Hisaki planetary space telescope. Although this instrument could not provide spatial resolution, they showed that the behavior changed over time, which they attributed to different auroral regions becoming dominant.

The first spectral maps of the FUV Jovian aurora were built using data collected in 2014 with the Space Telescope Imaging Spectrograph on board HST by Gérard et al. (2014). During the time-tagged spectral observations, the telescope was slewed so that the slit projection scanned the disk from above the polar limb down to mid-latitudes. Maps of the FUV color ratio showed that the amount of absorption by methane significantly varies between the different parts of the main aurora and the high latitude regions inside the main emission. They indicated that the highest color ratio, thus the hardest auroral precipitation,

occurs within the polar emissions and along the main oval. They also showed that auroral regions of strong electron precipitation do not necessarily coincide with the highest electron energies. Using model atmospheres adapted to auroral conditions combined with an electron transport model, the authors mapped the distribution of the characteristic electron energies and concluded that electrons characteristic energies range from a few tens to several hundred keV, depending on the region of the aurora concerned. They also stressed that uncertainties on the vertical distribution of methane limit the conversion from color ratio to characteristic electron energies.

It has been suggested that the relatively strong main auroral emission corresponds to the upward branch of a global current system flowing along magnetic field lines. This concept, initially introduced by Hill (2001) and Cowley and Bunce (2001) could explain the basic features of the main auroral emission. It was later refined by Nichols and Cowley (2004) by including a dependence of the ionospheric Pedersen conductivity modified by the precipitating electrons. In Jupiter's magnetosphere the current system giving rise to the main emission is associated with the transfer of planetary angular momentum to the magnetospheric plasma. This current system forms a narrow ring of upward field aligned current surrounding the magnetic pole. The current density in the ionosphere exceeds by far the maximum value that can be carried by unaccelerated magnetospheric electrons. Consequently, the electrons must be strongly accelerated along magnetic field lines from a few keV up to energies of several hundred keV, as was suggested by models (Cowley and Bunce, 2001; Cowley et al., 2003; Nichols and Cowley, 2004; Ray et al., 2012). Cowley and Bunce (2001) related the energy flux and the mean energy of the precipitating electrons using the Knight (1973) linear approximation in the case of an isotropic Maxwellian distribution of the source electrons linking the vertical current density to the field-aligned potential. Color ratio measurements based on HST spectra confirmed the presence of the energetic auroral

electrons in the Jovian main aurora (Gustin et al., 2004) and in the high-latitude emission (Gérard et al., 2003).

The dominant precipitation processes may be different for other components of the Jovian aurora. For example, pitch angle scattering of energetic electrons may be the main source of the diffuse aurora located equatorward of the main oval (Tomas et al., 2004; Radioti et al., 2009). Rapidly varying and flaring structures are observed at high latitude inside the main emission (Waite et al., 2001; Grodent et al., 2003; Bonfond et al., 2011). Their origin and acceleration process are still largely unknown. Finally, magnetic footprints of the Galilean satellites on the Jovian atmosphere appear to be generated by a parallel electric field associated with the propagation of Alfvèn waves (Jones and Su, 2008; Hess et al., 2013). It is very likely that the characteristic electron energy associated with these various processes is different, but it is currently largely unknown. In these cases, a defined relation between electron energy and auroral brightness is not necessarily expected.

In this study, we examine the relationship between the intensity of the unattenuated H_2 auroral emission and the FUV color ratio, used as a proxy of the characteristic energy of the electrons reaching the Jovian atmosphere. The primary objective is to determine whether organized relations are observed between the precipitated electron energy flux and the FUV color ratio for different components of the aurora. We separate the aurora into components such as the main emission, the equatorward diffuse emission and the high latitude emissions inside the main aurora and examine the relation between the H_2 emission intensity and the ultraviolet color ratio. For this purpose, we use the two-dimensional maps of the FUV color ratio obtained from the observations performed with HST in 2014.

2. Data processing

The data processing of the HST-STIS spectral images collected on 8 and 14 January, 15 March 2014 in the north, and 12 January in the south has been described by Gérard et al. (2014). In this study, we do not use the 14 January data for which the large value of the central meridian longitude only provides degraded visibility. In short, the HST observations were obtained with the STIS FUV-MAMA imaging spectrograph in January and March 2014 under different central meridian longitudes. The Space Telescope was slewed to move the slit projection across the polar regions while collecting FUV auroral spectra. The time-tagged spectral mode was used with the G140L grating, giving a spectral resolution of ~1.2 nm. The width of the 0.5 arcsec slit aperture subtends a perpendicular distance on the order of 1600 km during the time of these observations, corresponding to ~1.3 degree of latitude at the equator. Table 1, adapted from Gérard et al. (2014), lists the dates, times and central longitudes of the four visits performed in the frame of HST program 13402. The spectral observations lasted approximately 42 minutes during each visit. The integration time spent on each pixel depends on the angular amplitude of the slit scan. In these observations, it varies between 5 and 7 seconds.

Starting from the time-tag event lists, we constructed and calibrated a series of successive two-dimensional spectra. For each HST visit, we built images in the short (123-130 nm) and long (155-162 nm) wavelength domains corresponding to the terms in the definition of the color ratio. Finally, each spectral image is smoothed over 5x5 spatial pixels. As the HST spatial scans took several tens of minutes, the different latitudes were not observed simultaneously and these images cannot be considered as auroral snapshots. We only retain those pixels where the signal in both short and long wavelength domains exceed 2 kR following smoothing to reject data with too low signal to noise ratio. The fraction of excluded pixels is variable for each component of each image. For example it is on the order

of 30% in panels of Figure 5.

The color ratio map is finally obtained as the pixel-to-pixel ratio of the long to short wavelength images. The intensity measured in the 155-162 nm spectra band is converted into a total H_2 UV brightness using the fraction of photons emitted in this spectral band relative to the total emission in the unabsorbed laboratory H_2 spectrum by Dziczek et al. (2000).

3. Auroral electron flux - color ratio relation

Previous studies of the relationship between the auroral electron energy and the auroral brightness of the main emission associated with field aligned currents largely rest on the work by Knight (1973) and its variants. He developed a formula linking the intensity of the field-aligned current carried by precipitating electrons and the field-aligned potential in terrestrial auroral arcs in the case of an initial Maxwellian isotropic distribution. When the required current density considerably exceeds the maximum for the unaccelerated electron population, the current density depends quasi-linearly on the accelerating potential and the kinetic energy flux increases as its square. In the formulation by Cowley and Bunce (2001), based on Knight's kinetic theory of field-aligned currents and its application by Lundin and Sandahl (1978) and Lyons (1980), the precipitated energy flux may be related to the energy of the electrons accelerated by a field-aligned voltage. As described in details in Gustin et al. (2004), the field-aligned voltage $\Phi_{//}$ required to produce a current density $j_{//i}$ larger than $j_{//i0}$ the maximum ionospheric current density that can be carried by precipitating magnetospheric electrons without field-aligned acceleration may be approximated by

$$e\Phi_{\parallel} = W_{th}\left[\left(\frac{j_{\parallel i}}{j_{\parallel i0}}\right) - 1\right] \quad , \qquad (2)$$

with

$$j_{\parallel i0} = eN\left(\frac{W_{th}}{2\pi m_e}\right)^{1/2} \qquad (3)$$

where e and m_e are the charge and mass of the electron, and N and W_{th} are the number density and thermal energy of the 'source' magnetospheric electron population, assumed to have an isotropic Maxwellian distribution. In this expression, it has been assumed that the potential drop is significantly larger than W_{th}, that the acceleration region is limited in extension so that no particle mirrors before experiencing the full voltage drop, and that the 'top' of the voltage drop occurs well above the minimum height r_{min}. As discussed by Cowley and Bunce (2001), this altitude is given approximately by $(r_{min}/R_J) \approx (j_{\|i}/j_{\|i0})^{1/3}$, assuming a dominant dipole planetary field in the polar regions.

The mean energy <W> of the precipitating electrons is then be given in terms of the energy flux E_{fi} by:

$$\langle W \rangle = 2W_{th} \frac{\left(\frac{E_{fi}}{E_{fi0}}\right)}{\left(2\left(\frac{E_{fi}}{E_{fi0}}\right)-1\right)^{1/2}} \qquad (4),$$

where $E_{fi0} = 2NW_{th}\left(\frac{W_{th}}{2\pi m_e}\right)^{1/2}$ is the field-aligned energy flux in the absence of potential drop.

Cowley (2006) extended the relationship to the case of relativistic accelerating potentials and showed that the energy flux carried by the electrons then increases as the cube of the potential, rather than as the square. Ray et al. (2009) used a different analytical current choke formula based on a Vlasov model where the current density (hence the number flux) saturates for increasing potential drop. Ray et al. (2010) showed that the field-aligned potentials in the jovian system are a significant fraction of the rotational potential and need to be self-consistently treated when describing the current system associated with angular momentum transport. They showed that the rapid rotation centrifugally confines heavy ions to the equatorial plane, resulting in an ambipolar electric field that restricts the mobility of the magnetospheric electrons. A field-aligned potential drop develops at high latitudes and the

nature of the field aligned current-voltage relation is controlled by the plasma population and the magnetic field strength at this location. They showed that the accelerating potential energy strongly depends on the location of the acceleration region, a quantity still largely unknown. Only the upward current system was described by the Ray et al. (2010) model. Therefore, their model requires an outer constraint to select a solution. Figure 3 in Tao et al. (2016) compared various forms of the energy flux-mean electron energy relation.

Formula (4) may be adapted to relate the total unabsorbed H_2 emission rate (in kR) to the electron energy flux (in mW m^{-2}). The conversion factor is based on results of electron transport models showing that ~10 kR of Lyman (B→X) and Werner (C→X) H_2 band emission is produced for a 1 mWm^{-2} electron precipitation, over a wide range of initial electron energies. Using this factor and expression (4), Figure 1 illustrates the relation between the unabsorbed vertical H_2 intensity and the electron mean energy given by equations (3) and (4). The curves are plotted for an initial thermal electron energy W_{th} of 2.5 keV and three different electron densities N in the equatorial plane between 0.001 and 0.01 cm^{-3} to cover the expected density range in the equatorial plane. A value N = 0.003 cm^{-3} provided the best fit in an earlier study of the observed intensity-color ratio relation for the main auroral emission (Gustin et al., 2004).

4. Results

We first look for possible relation between the brightness of the auroral pixels and the corresponding color ratio using the full set of auroral pixels, including the Io footprint and its trailing tail. The data points in Figure 2 show the color ratio and the total H_2 intensity of all auroral pixels for the observations on 8 January 2014 in the northern hemisphere. In this context, auroral pixels include all the auroral emission, along and poleward of the Io reference oval.

The total H_2 emission is derived from the brightness observed in the unabsorbed 155-162 nm spectral window by scaling it to the total H_2 emission calculated for a synthetic spectrum of H_2 excited by energetic electrons. It includes emissions from the B, C, D, B', C' and B" singlet states to the ground state. It was shown that laboratory (Dziczek et al. 2000) and Jovian and Saturnian auroral spectra are well fitted by the synthetic spectra (Gustin et al., 2013). Figure 2 clearly shows a wide range of color ratios, up to more than 20, while the total H_2 brightness reaches as much as 8500 kR. Some CR data points are less than 1.1, the value for unabsorbed H_2 emission. These are associated with low measured intensities close to our 2 kR limit, when the signal to noise ratio is lower. We also note that only relatively low brightness values are associated with low color ratios. The limit defining the minimum observed intensity increases steadily with the color ratio up to CR~7. A wide range of scatter is observed between the two quantities, but structures appear in the plot, suggesting that several different populations are mixed with different relational characteristics. A similar dispersion was obtained for the images of 12 January and 15 March. Therefore, the scatter suggests to separate the aurora into several components and examine their individual color ratio-brightness relation This is shown in Figure 3 for the 8 January reconstructed images, where seven regions have been defined in the spectral images as shown in panel a). They correspond respectively to (b, in blue) the stripes observed along the main auroral oval in the morning sector (see Gérard et al., 2014); (c, in purple) the main emission in the dusk sector; (d, in green) the outer (equatorward of the main emission) aurora in the morning sector; (e, in yellow) the outer (equatorward of the main emission) aurora in the dusk sector; (f, in orange) the bright polar emission; (g, in red) the second region of polar emission and (h, in brown) the Io footprint. The contours of the different regions in this and the following plots were made visually, also guided by the characteristics of the two-dimensional color ratio maps shown by Gérard et al. (2014) for the same images. We note that both (f) and (g) regions are part of the

active region described by Grodent et al. (2003) on the basis of their dynamical behavior observed with STIS in the timetag mode.

The grey dots in each panel correspond to the global plot shown in Figure 2. Panels b) to h) in Figure 3 show that different regions exhibit distinct intensity-color ratio characteristics. For all seven regions, we fit a linear regression between the CR and the H_2 emission brightness. Table 2 lists the slope p and the correlation coefficient R of each fit. In addition, to estimate the scatter, we first order the data points in each auroral component by increasing auroral intensity. We then divide the sample into j_{max} bins containing the same amount of data points and calculate the chi-square expression:

$$\chi^2 = \frac{1}{j_{\max}} \sum_{j=1}^{j_{\max}} (1/i_{\max}) \sum_{i=1}^{i_{\max}} \left(CR_{i,j} - \mu_j \right)^2 \qquad (5)$$

where μ_j is the mean value of the color ratio in bin j, $CR_{i,j}$ are the values of the color ratio in bin j, i_{max} the equal number of data points in each intensity. The values listed in Table 2 for this and the other two images were obtained for j_{max}=10. We checked that the value of $\chi 2$ is nearly independent of the number of bins j_{max}.

The main emission stripe region (panel b, in dark blue) includes the brightest auroral emission along the main oval in the morning sector. Most pixels correspond to color ratios between 1 and 8 and spatially the highest intensities correspond to the highest color ratio (Gérard et al., 2014). The slope is quite low: p=0.2 CR unit/MegaRayleigh and an indication of saturation at intensities higher than ~4000 kR is observed. The region of the dusk main oval (panel c, in purple) shows similar characteristics, with a grouping of the data points along a straight line with a slope higher than in panel b). The correlation coefficient R is equal to 0.79, the highest of the seven R values for this image and the χ^2 is among the low observed values. The outer emission regions (equatorward of the main emission) in the dawn (panel d, in green) and dusk (panel e, in yellow) sectors are characterized by an extended

range of CR values associated with a relatively low brightness. Region d) appears to show two branches, and it has the largest χ^2 of all zones in all three images and the lowest correlation coefficient observed on 8 January. The outer emission on the dusk side e) shows the highest slope value and its chi-square is less than for the morning outer emission. The first region of polar auroral emission (f) includes most of the pixels with the highest CR, some reaching values over 20. It was associated with electron energies in the range 300-450 keV by Gérard et al. (2015), depending on the adopted atmospheric model. It corresponds to the second highest linear correlation coefficient. In the polar stripe region (g), both the ranges of intensities and CRs are limited to smaller values, which partly explain the small χ^2 value. Finally, the Io footprint and tail (h) mostly show low brightness and small CRs, as was found in earlier CR studies of the satellite footprint and tail (Dols et al., 2000; Gérard et al., 2002, 2014). However, the color ratio is larger than the unabsorbed value of 1.1, which suggests that some absorption is taking place above the auroral emission. This result is in contrast with the study of limb UV images that lead to the conclusion that the footprint emission originates from an altitude of at least 550 km (Bonfond et al., 2009), far above the expected region of significant hydrocarbon absorption.

Figure 4 concentrates on regions (b) and (f) and illustrates the dichotomy between the main emission and the bright polar region. A better defined relationship is seen along the bright morning side of the main emission. In this region, intensity striations are observed along the main emission, with a limited dispersion in the relation between the H_2 brightness and the CR. Remarkably, most CR values lie below those of the polar flare emission, indicating a lower auroral electron energy precipitation in the main emission. A statistical increase of the CR is also observed for the bright polar flare but the relation between the two quantities is clearly different for the two populations, as evidenced by the large difference between the corresponding chi-square values of 1.7 and 4.6 respectively.

Figures 5 and 6 confirm the contrast between the different regions observed on the other dates. The spectral image was collected on 15 March 2014 in the north for a central meridian longitude ~50° larger than shown in Figures 2, 3 and 4. The boundaries of the six auroral features, grouped into four main auroral components, is shown in Figure 5a. In this image, the main emission more clearly extends along most of the dayside than in Figure 3a and is visible over almost 360° into the nightside. The selected regions are: (b, in dark blue) the extended dayside main emission (c, in green and red) the lower dusk ansa of the main emission, (d, in yellow and orange) the dawn and dusk and outer emissions (equatorward of the main emission) and (e, in purple) the polar region. The dayside main emission (b) shows a low-scatter relation between the brightness and the color ratio. The plot of the main emission dusk ansa (c) indicates that the color ratio varies quasi linearly with the auroral brightness in this region. As two different slopes are observed in the plot, we have examined to what substructure the two sets of data point belong. This analysis shows that the lower branch in the plot (in green) corresponds to the upper part of the ansa, while the other branch (in red) includes the pixels belonging to the lower part of the ansa. Both show a clear CR-brightness relation with linear correlation coefficients as high as 0.80 and χ^2 equal to 0.2 and 0.5 and slopes p=1.1 and 2.0 CR unit/MR. The next panel d) corresponds to the outer (dawn and dusk) emissions and shows widely scattered data points. Table 2 indicates that the two sub-regions have similar χ^2 and R values, but the slope p in the dawn sector is twice that of the dusk sector. Finally, the polar emission (e) has the largest range of CR values (up to ~17), with a steep CR-brightness relation. Figure 6 clearly demonstrates the different relations observed in the region of the main emission ansa at dusk and in the polar auroral structure. Remarkably, the slope for the main emission ansa in the linear least-squares regression is significantly less (p =1.1) than that of the polar emission (p = 16.6), similarly to Figure 4.

Finally, Figure 7a shows the six auroral features grouped into four main components identified in the exposure obtained on 8 January 2014, the only spectral image of the southern aurora obtained so far. As the viewing geometry from Earth orbit is less favorable for the south, structures are not as easily separated as in the previous two cases. Some of the emission is observed close to or even beyond the limb. The exclusion of those pixels close to the limb did not substantially modify the relations described below in the different regions. This is in agreement with Figure 5 by Gérard et al. (2014) which does not show an appreciable change in the observed color ratio across the limb. We define: the region of the dusk ansa of the main emission (panel b, in purple), the region of the dawn ansa of the main emission (panel c, in yellow and violet), the dusk (in red) and dawn (in green) outer emissions (panel d) and the polar emission region (panel e, in orange). The dusk ansa of the main emission (b) has the smallest slope value p=0.1) of the regions of all three images. A plateau at the level CR=2 is observed above ~500 kR. The dawn ansa (component c) suggests a relation between the CR and the auroral intensity, characterized by the highest of the main emission components (R=0.83). As two different populations appeared to be present, we have divided the dawn ansa into two sub-structures, the brightest emission blob (yellow points) and the secondary blob (violet points). The former zone is associated with a number of higher CR values indicating a harder precipitation than the secondary region. Similarly, panel d) compares the outer diffuse emission divided into a dawn component (in green dots) and a dusk region (red dots). The first one shows higher CRs and a more pronounced dependence (p=10.3) versus the brightness of the auroral intensity than the second one (p=1.4). Globally, we note that the highest color ratio values in this image of the south aurora are those observed inside the dawn ansa. Finally, panel e) shows a relatively low χ^2 value for the polar region. It is also noteworthy that the distribution of data points is quite different from that shown in Figure 5(f), although they correspond to roughly similar polar regions.

5. Discussion

This study indicates that no global relation between the precipitated electron flux and the electron mean energy, represented by the UV color ratio is observed. Dividing the aurora into specific regions demonstrates that they exhibit different relations, probably suggesting different precipitation regimes. A color ratio-brightness is more clearly present in some of the components of the jovian aurora. The main auroral ring appears to show relatively high correlation. It is associated with the upward branch of the global current linking the magnetosphere and the ionosphere and shows a well organized relation as shown in Figures 4 and 6 and confirmed by Table 2. Region (b) on March 15 as defined in Figure 5a corresponds to a smaller correlation coefficient than in other zones of the main emission, possibly because it includes a wide range of longitudes and local times with different electron characteristics.

The high latitude vertical distribution of hydrocarbons in the aurora is poorly constrained. Therefore, the color ratio-electron energy relation depends on the CH_4 vertical distribution, as was shown by Gérard et al. (2014). In addition, the relation between the precipitated energy flux and the H_2 brightness as observed from HST depends on the three-dimensional structure of the auroral morphology which is only loosely constrained. Therefore we do not find it appropriate to quantitatively compare the relationship in Figure 1 which is established for nadir with those described in Figures 2 to 7.

The color ratio of the Io footprint and its tail remain relatively low, but higher than the unabsorbed value, as was confirmed by the studies by Gérard et al. (2002, 2014) and Gustin et al. (2016). It is probably excited by electrons accelerated by inertial Alfvén waves (Hess et al., 2013). The discrepancy between the presence of moderate methane absorption of the shorter wavelength emission and the altitude determination from analysis of limb images was

analyzed and discussed by Bonfond et al. (2009).

The process accelerating the electrons (and/or ions) causing the polar emission is probably quite different from the precipitation processes generating the main emission. Bright polar flares have been repeatedly observed reaching an intensity not usually found elsewhere. These flares correspond to a rapid brightness increase by as much as a factor 30, reaching peak brightness as high as 40 MR (Waite et al., 2001). Bonfond et al. (2011) reported observations of a recurrent flare, with a characteristic timescale of 2-3 minutes. Using the magnetic flux mapping model by Vogt et al. (2011), they found that this region mapped to radial distance ranges from 55 to 120 Jovian radii and suggested that these quasi-periodic auroral flares were possibly related to pulsed reconnections at the dayside magnetopause.

High values of the color ratio (and the mean electron energy) were observed at high latitudes in association with the bright polar emission as can be seen in Figures 3 and 4. Unlike in the main auroral emission, Gérard et al. (2003) found no relationship between the electron energy flux and the color ratio measured with STIS during time variations of ultraviolet high-latitude polar flares. They concluded that the mechanism causing these polar flares does not increase the energy of the precipitated electrons, but it enhances their number flux. They suggested that pitch angle scattering into the loss cone by magnetic pumping of energy perpendicular to the field lines following magnetic field compression as a possible process explaining these features. However, no definite conclusion was drawn concerning the process leading to the energization of electrons precipitating at high latitude. This is also the active region where Branduardi-Raymont et al. (2008) observed X-ray emission consistent with precipitation of highly stripped ions. The mechanism appears complex as spectroscopy indicates that sulfur and oxygen ions are also precipitated into the high latitude upper atmosphere (Bhardwaj and Gladstone, 2000; Branduardi-Raymont et al., 2008; Ozak et al., 2013). The high latitude X-ray source is a K-shell emission mechanism caused by

precipitation of heavy ions with energies of several MeV energy. These ions appear to originate in the outer magnetosphere, possibly penetrating during magnetic reconnection events between the planetary and the solar wind magnetic fields and accelerated to MeV energies by potentials along field line in the outer magnetosphere.

The diffuse emission equatorward of the main emission is presumably excited by electrons precipitated by a different process. Electron scattering and precipitation resulting from wave particle interactions in a broad region of the magnetosphere (10 to 25 R_J) was suggested as a possible source of equatorward diffuse emission by Bhattacharya et al. (2001) and Tomas et al. (2004). Radioti et al. (2009) described diffuse ultraviolet auroral emission observed with Hubble equatorward of the main emission. Using simultaneous HST FUV and Galileo wave and electron data, they demonstrated that electron scattering into the loss cone by whistler mode waves can induce a precipitated energy flux large enough to account for the auroral emissions. In the polar region and equatorward regions, no known simple relationship between the auroral brightness and the electron energy has been modeled. The lack of an organized relation for most of the equatorward diffuse and the polar emissions in Figures 3, 5 and 7 suggest that such a relation may not exist.

6. Conclusions

Analysis of the ultraviolet spectral images obtained in 2014 with the Hubble Space Telescope demonstrates that no global color ratio-energy flux relation is found when Jovian auroral UV emissions from all auroral components are analyzed as one single dataset. The relationship between the intensity of the H_2 emission and the UV color ratio changes between regions such as the main emission, the Io magnetic footprint, the diffuse aurora and the polar emission inside the main emission ring. However, all components indicate a statistical trend

of increasing color ratio (harder electron precipitation) associated with higher auroral intensity (higher precipitated energy flux). The electron density in the equatorial plane probably varies with latitude and local time, at least partly explaining differences between slopes in the panel plots and some of the data scatter when the selected components include a range of local times and latitudes as was seen in Figure 5d.

The color ratio (and thus the electron mean energy) of the Io footprint and trailing tail is low compared to other auroral components. This is in agreement with previous spectral studies consistently showing that the Io footprint and its tail have a lower color ratio than any other part of the jovian auroral emission. The diffuse equatorward aurora does not reveal a clear relation between the electron energy flux and the energy of the electron precipitation. Similarly, in the polar emission, the amount of absorption by hydrocarbons does not appear clearly related to the intensity of the electron precipitation. This conclusion is in agreement with previous observations of time variations of polar spots indicating that most of the intensity enhancements are caused by an increase of the electron number flux rather than by an increased electron mean energy.

The intensity of main emission generally shows an organized variation with the electron energy, as was previously shown for local measurements of the color ratio observed at fixed preset locations along the main emission. This is also in qualitative agreement with the linear Knight or other expressions linking the mean electron energy accelerated by a potential drop along the magnetic field lines to the field aligned current intensity. The lack of such clear relationship in other auroral components suggests that the electron energization processes at work in the diffuse and high latitude aurora probably does not necessarily imply the presence of field-aligned currents.

Acknowledgements. *B.B. acknowledges support from the Belgian Fund for Scientific Research (FNRS). Funding for this research was provided by the PRODEX program of the European Space Agency, managed in collaboration with the Belgian Federal Science Policy Office. This research is based on observations with the NASA/ESA Hubble Space Telescope, obtained at the Space Telescope Science Institute, which is operated by AURA for NASA. It is based on observations acquired with the NASA/ESA Hubble Space Telescope (program ID 13402), and may be obtained from the Space Telescope Science Institute (https://archive.stsci.edu/hst/search.php). The authors than the reviewers for their useful comments.*

REFERENCES

Ajello, J. et al. 1998. Galileo orbiter ultraviolet observations of Jupiter aurora. J. Geophys. Res. 103, 20125-20148, 10.1029/98JE0083.

Badman, S. V., et al., 2014. Auroral processes at the giant planets: energy deposition, emission mechanisms, morphology and spectra. Space Science Reviews 187, 99-179, doi: 10.1007/s11214-014-0042-x.

Bhardwaj, A., Gladstone, G. R., 2000. Auroral emissions of the giant planets. Rev. Geophys. 38, 295–353, doi:10.1029/1998RG000046.

Bhattacharya, B., et al., 2001. On the energy source for diffuse Jovian auroral emissivity. Geophys. Res. Lett. 28, doi: 10.1029/2000GL012616.

Bonfond, B. et al., 2009. The Io UV footprint: Location, inter-spot distances and tail vertical extent. J. Geophys. Res. 114, A07224, doi:10.1029/2009JA014312.

Bonfond, B. et al., 2011. Quasi-periodic polar flares at Jupiter: A signature of pulsed dayside reconnections? Geophys. Res. Lett. 38, L02104, doi:10.1029/2010GL045981.

Bonfond, B. et al., 2015. The far-ultraviolet main auroral emission at Jupiter – Part 2: Vertical emission profile. Ann. Geophys. 33, 1211-1219, doi:10.5194/angeo-33-1211-2015.

Branduardi-Raymont, G. et al., 2008. Spectral morphology of the X-ray emission from Jupiter's aurorae. J. Geophys. Res. 113, A02202, doi:10.1029/2007JA012600.

Clarke, J.T. et al., 2004. Jupiter's aurora, in: Bagenal, F., Dowling, T.E., McKinnon W.B., Jupiter. The planet, satellites and magnetosphere. Cambridge planetary science, Vol. 1. Cambridge University Press, Cambridge, UK, 639 – 670, ISBN 0-521-81808-7.

Cowley, S.W.H. (2006). Current-voltage and kinetic energy flux relations for relativistic field-aligned acceleration of auroral electrons. Annales Geophysicae 24, 325–338, 2006, doi : 1432-0576/ag/2006-24-325.

Cowley, S.W.H., Bunce, E.J., 2001. Origin of the main auroral oval in Jupiter's coupled magnetosphere-ionosphere system. Planet. Space Sci. 49, 1067.

Cowley, S.W.H. et al., 2003. Origins of Jupiter's main oval auroral emissions. J. Geophys. Res. 108, 8002, doi:10.1029/2002JA009329.

Dziczek, D., et al. 2000. Cascade contribution to the H_2 Lyman band system from electron impact. Physical Review A, 61, 064702.

Dols, et al. 2000. Diagnostics of the Jovian Aurora Deduced from Ultraviolet Spectroscopy: model and HST/GHRS Observations. Icarus 147, 251-266, doi: 10.1006/icar.2000.6415.

Gérard, J.-C. et al. 2002. Excitation of the FUV Io tail on Jupiter: Characterization of the electron precipitation, J. Geophys. Res. 107, 1394, doi:10.1029/2002JA009410.

Gérard, J.-C. et al. 2003. Spectral observations of transient features in the FUV Jovian polar aurora. J. Geophys. Res. 108, 1319, doi:10.1029/2003JA009901.

Gérard, J.-C. et al., 2014. Mapping the electron energy in Jupiter's aurora: Hubble spectral observations. J. Geophys. Res. 119, doi:10.1002/2014JA020514.

Grodent, D. et al. 2003; Jupiter's polar auroral emissions, J. Geophys. Res. 108, 1366, doi:10.1029/2003JA010017.

Gustin, J. et al. 2004. Energy-flux relationship in the FUV Jovian aurora deduced from HST-STIS spectral observations, J. Geophys. Res. 109, A10205, doi:10.1029/2003JA010365.

Gustin, J., et al. 2016, Characteristics of north Jovian aurora from STIS FUV spectral images, Icarus, 268, 215-241, doi: 10.1016/j.icarus.2015.12.048.

Hess, S. et al. 2013. Evolution of the Io footprint brightness II: Modeling. Planet. Space Sci. 88, 76–85, doi: 10.1016/j.pss.2013.08.005.

Hill, T. W. 2001. The Jovian auroral oval. J. Geophys. Res. 106, 2156-2202, doi: 10.1029/2000JA000302.

Jones, S. T., Su Y.-J. 2008. Role of dispersive Alfvén waves in generating parallel electric fields along the Io-Jupiter fluxtube. J. Geophys. Res., 113, A12205, doi:10.1029/2008JA013512.

Knight, S. 1973. Parallel electric fields. Planet. Space Sci. 21, 741–750, doi:10.1016/0032-0633(73)90093-7.

Livengood, T.A., Moos, H.W. 1990. Jupiter's north and south polar aurorae with IUE data. Geophys. Res. Lett. 17, 2265–2268, doi:10.1029/GL017i012p02265.

Lundin, R., Sandahl, I. 1978. Some characteristics of the parallel electric field acceleration of electrons over discrete auroral arcs as observed from two rocket flights, Symposium on European Rocket Research, Ajaccio, Rep. ESA SP-135, p. 125, European Space Agency, Noordwijk, Netherlands, 1978.

Lyons, L. 1980. Generation of large-scale regions of auroral currents, electric potentials, and precipitation by the divergence of the convection electric field, J. Geophys. Res., 85, 17–24, doi:10.1029/JA085iA01p00017.

Morrissey, P. F et al. 1997. Simultaneous spectroscopy and imaging of the Jovian aurora with the Hopkins Ultraviolet Telescope and the Hubble Space Telescope. The Astrophysical Journal 476, 918.

Nichols, J., Cowley S. W. H. 2004. Magnetosphere-ionosphere coupling currents in Jupiter's middle magnetosphere: Effect of precipitation induced enhancement of the ionospheric Pedersen conductivity. Ann. Geophys., 22, 1799–1827, doi: 10.5194/angeo-22-1799-2004.

Ozak, N. et al. 2013. Auroral ion precipitation at Jupiter: Predictions for Juno, Geophys. Res. Lett., 40, 4144–4148, doi:10.1002/grl.50812.

Radioti, A. et al. 2009. Equatorward diffuse auroral emissions at Jupiter: Simultaneous HST and Galileo observations. Geophys. Res. Lett. 36, L07101, doi:10.1029/2009GL037857.

Ray, L. C., Su, Y.-J, Ergun, R. E., Delamere, P. A., Bagenal, F. 2009. Current-voltage relation of a centrifugally confined plasma, J. Geophys. Res., 114, A04214, doi:10.1029/2008JA013969.

Ray, L.C. et al. 2010. Magnetosphere-ionosphere coupling at Jupiter: Effect of field-aligned potentials on angular momentum transport, J. Geophys. Res., 115, A09211, doi:10.1029/2010JA015423.

Ray, L.C. et al. 2012. Magnetosphere-ionosphere coupling at Jupiter: a parameter space study,

J. Geophys. Res., 117, A01205, doi:10.1029/2011JA016899.

Tao, C. et al. 2016. Variation of Jupiter's Aurora Observed by Hisaki/EXCEED: 2. Estimations of Auroral Parameters and Magnetospheric Dynamics. J. Geophys. Res. 120, doi:10.1002/2015JA021272.

Tomás, A.T. et al. 2004. Energetic electrons in the inner part of the Jovian magnetosphere and their relation to auroral emissions, J. Geophys. Res., 109, A06203, doi:10.1029/2004JA010405.

Vasavada, A. R., et al. 1999. Jupiter's visible aurora and Io footprint. J. Geophys. Res., 104(E11), 27133-27142.

Vogt, M. F. et al. 2011. Improved mapping of Jupiter's auroral features to magnetospheric sources, J. Geophys. Res. 116, A03220, doi:10.1029/2010JA016148.

Waite, J.H., Jr., et al. 2001. An auroral flare at Jupiter. Nature 410, 787.

Yung, Y. L., et al. 1982. H_2 fluorescence spectrum from 1200 to 1700 Å by electron impact: Laboratory study and application to Jovian aurora. Astrophys. J. 254, L65–69, doi:10.1086/183757.

Table 1: HST spectral scans of the Jovian FUV aurora used in this study

Date (2014)	Hemisphere	start UT	CML range*
Jan. 8	North	23:06	155°-188°
Jan. 12	South	22:43	24°-48°
Mar.15	North	18:34	207°-231°

*Range of S_{III} longitudes during the STIS auroral exposure

Table 2: Parameters of the auroral brightness – color ratio relation of auroral components in three ultraviolet spectral images.

	Standard deviation[3]	Slope[2] (CR unit /MR)	Correlation coefficient[3]
January 8 (North)			
Stripes	1.7	0.2	0.34
Dusk main emission	0.4	1.3	0.79
Morning outer emission	8.6	2.2	0.26
Dusk outer emission	1.7	7.0	0.50
Bright polar flare	4.6	3.7	0.66
Polar stripes	0.2	4.7	0.58
Io footprint	0.5	1.4	0.44
March 15 (North)			
Dayside main emission	0.8	1.8	0.59
Main emission ansa: Upper branch	0.5	1.1	0.80
Main emission ansa: Lower branch	0.2	2.0	0.80
Dawn outer emission	0.5	3.0	0.49
Dusk outer emission	0.6	1.5	0.44
Polar emission	2.0	15.6	0.74
January 12 (South)			
Dusk ansa	0.3	0.1	0.13
Secondary dawn ansa	4.6	6.7	0.83
Dusk outer emission	0.4	1.4	0.33
Dawn outer emission	0.8	10.3	0.71
Polar emission	0.2	1.4	0.49

[1] Standard deviation χ^2 of the ten binned CR values (see text)
[2] Slope of the linear regression for total H_2 brightness expressed in MegaRayleighs (MR)
[3] Correlation coefficient of the linear regression

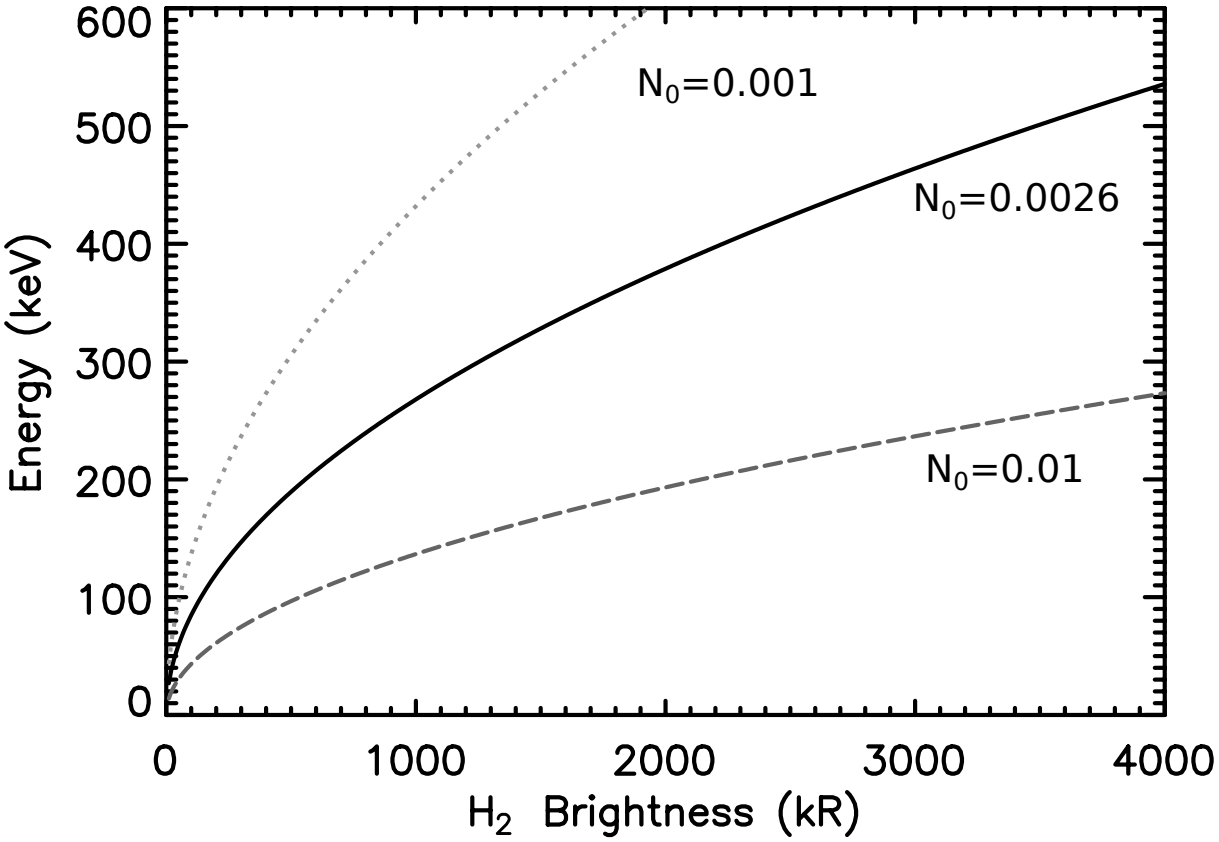

Figure 1: relation between the vertical brightness of the total unabsorbed H_2 emission rate for auroral electrons accelerated in a field-aligned current and the electron mean energy from equation (3). The parameters used for this plot are W_{th}= 2.5 keV and N=0.001, 0.0026 and 0.01 cm^{-3} (see text).

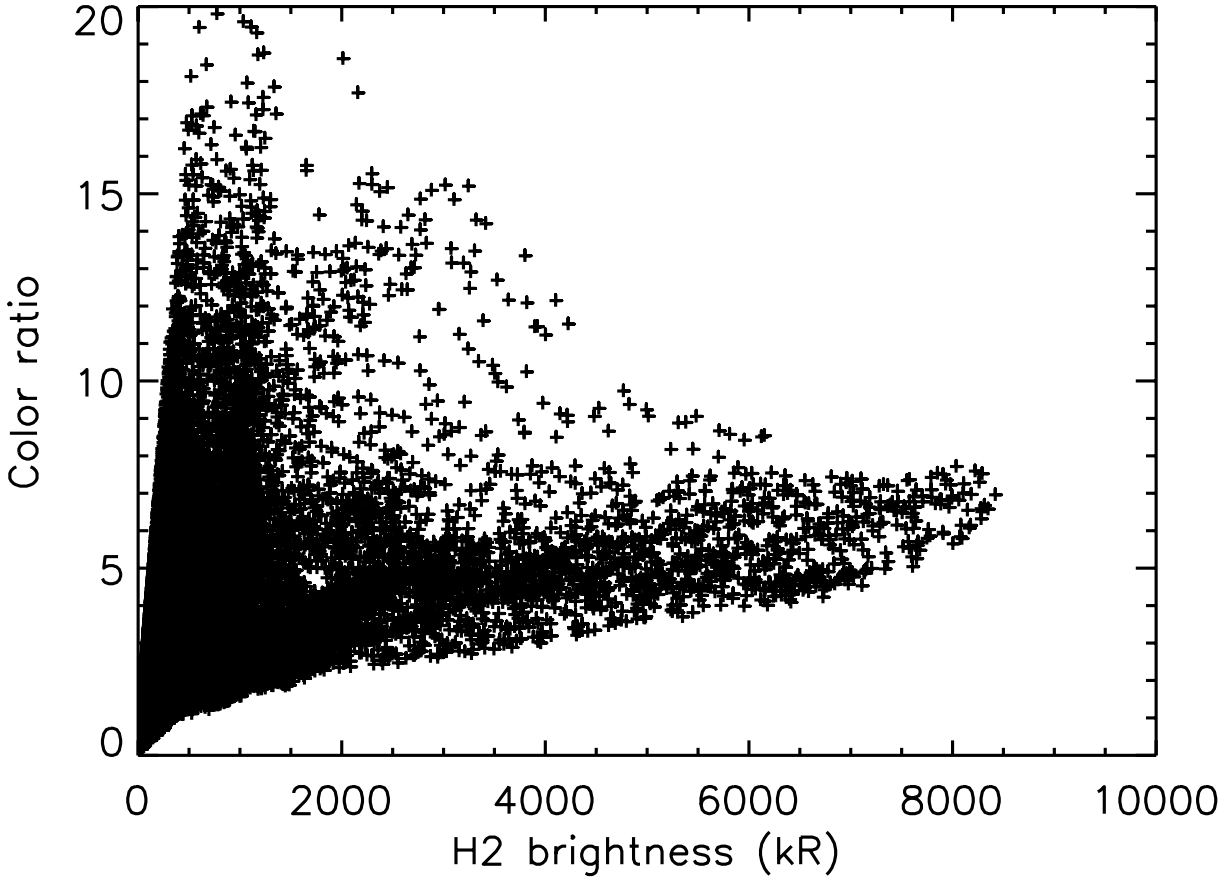

Figure 2: observed color ratio versus the emitted auroral brightness of the total H_2 emission using all spatial auroral pixels in the reconstructed spectral image of 8 January 2014.

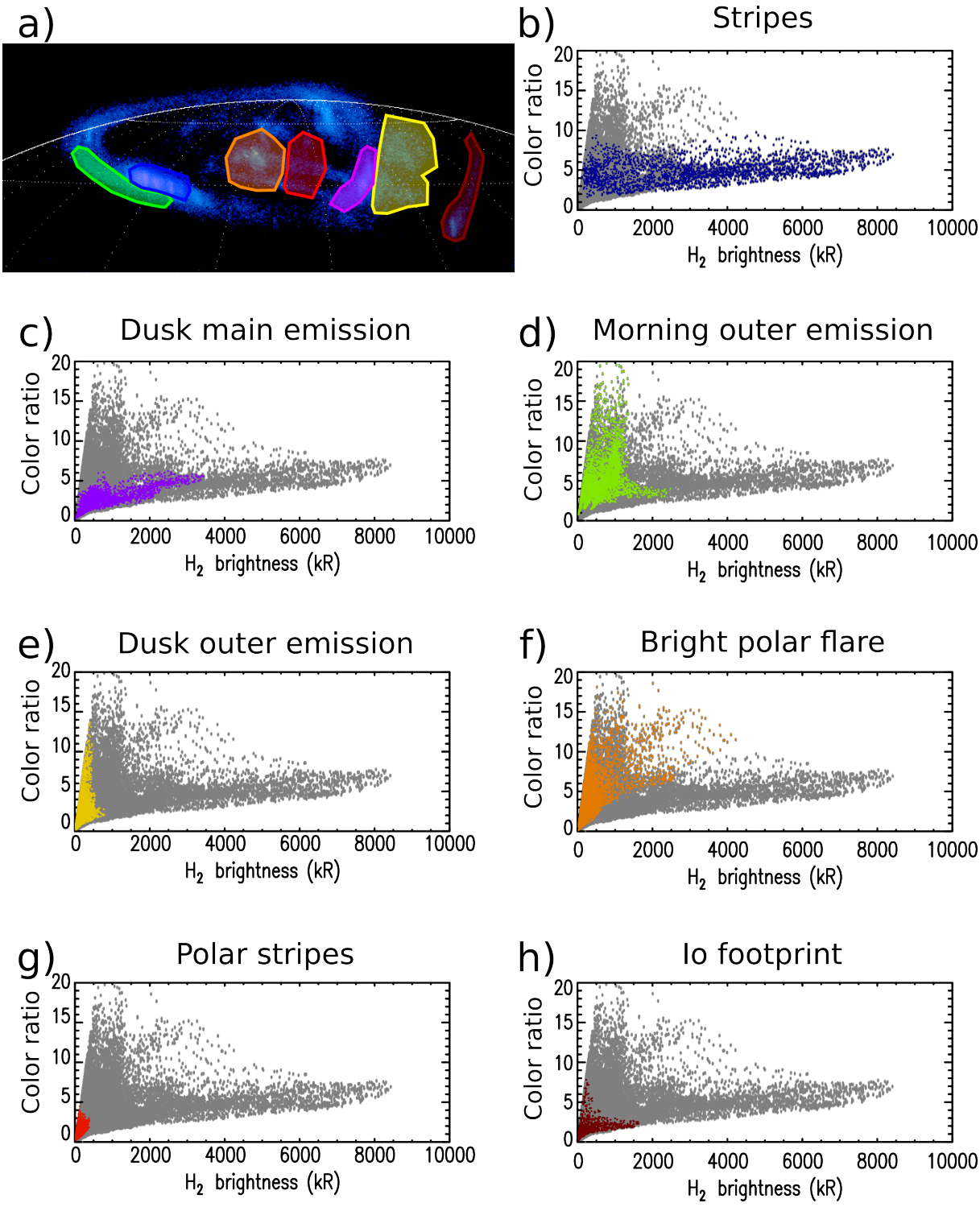

Figure 3:
Panel a): reconstructed image of 8 January 2014 in the North divided into auroral components. The position of the planetary limb at the 1 bar level is shown by the white solid line. The white dotted lines show the 75° and 60° north parallels and the meridians at 15° intervals. Panels b) to h): observed relationship between the FUV color ratio and the total UV H_2 auroral brightness emission. Different auroral regions have been selected as shown in panel a) with the colors corresponding to the different components. The grey background area corresponds to all auroral pixels

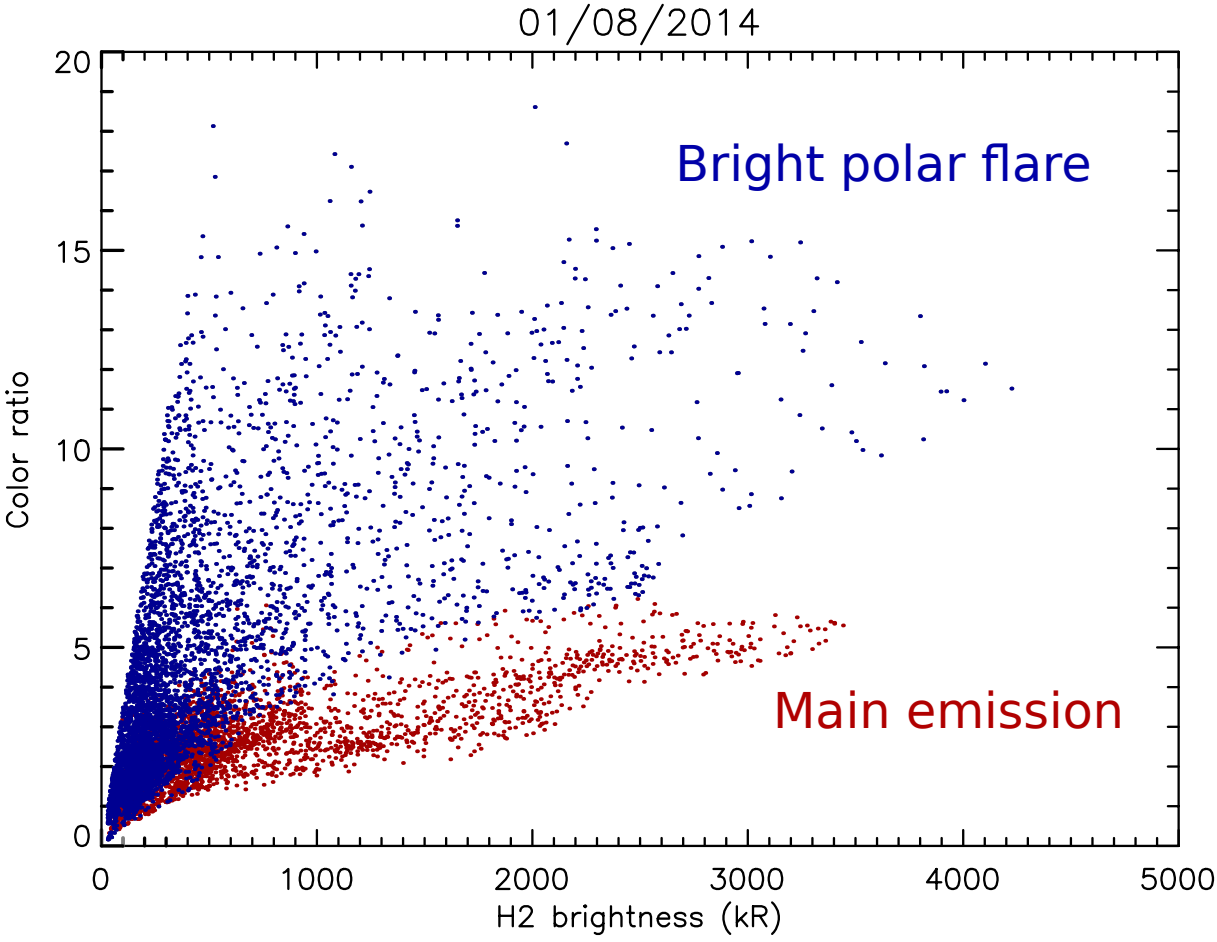

Figure 4: relationship between the FUV color ratio and the total UV H_2 auroral brightness measured on 8 January 2014 in the main emission (red dots) and bright polar flare (blue dots) regions.

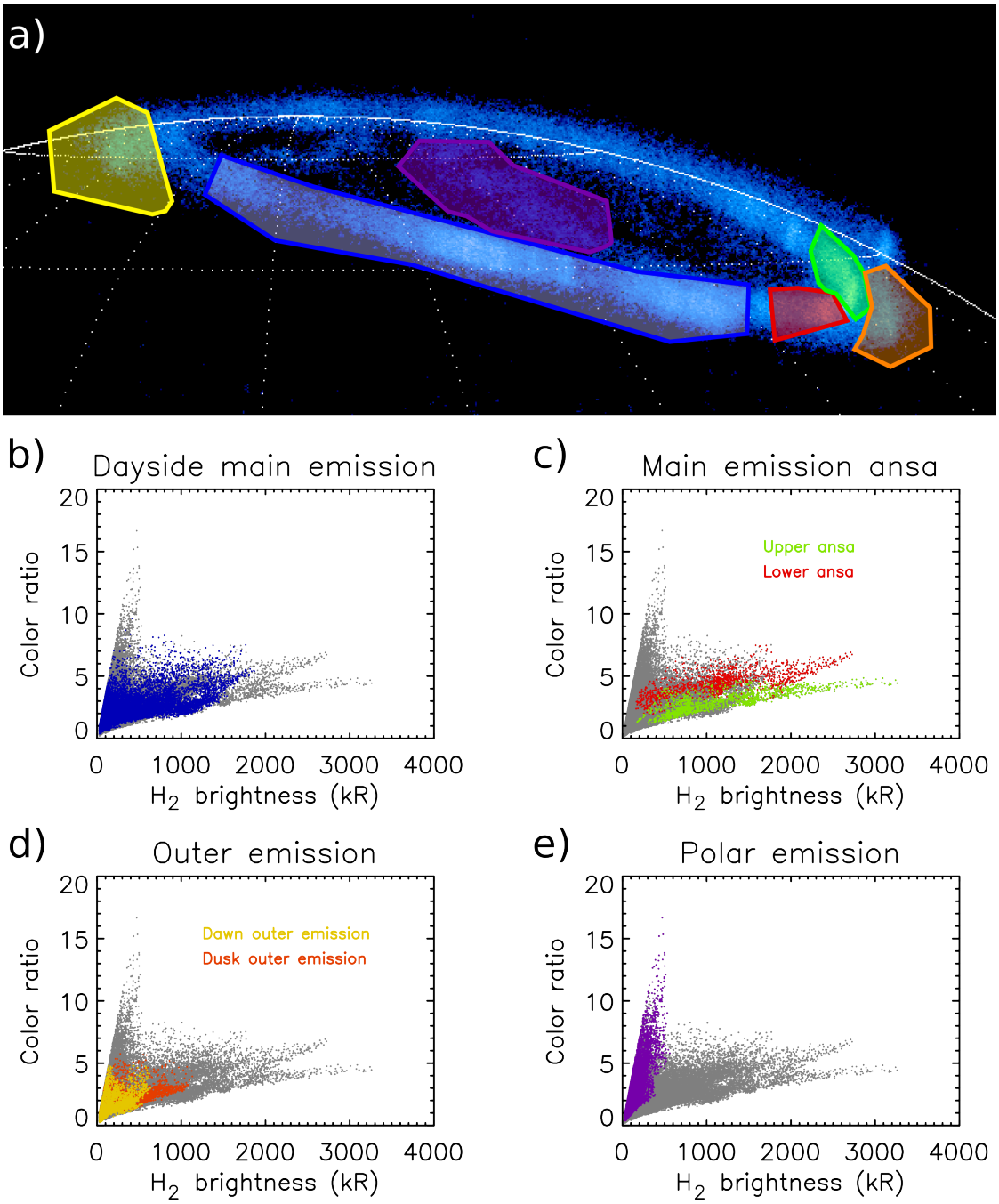

Figure 5:
a) reconstructed image of 15 March 2014 divided into auroral components. The position of the planetary limb at the 1 bar level is shown by the white line.
The white dotted lines show the 75° and 60° north parallels and the meridians at 15° intervals. Panels b) to e): observed relationship between the FUV color ratio and the total UV H_2 auroral brightness emission. Several auroral regions have been selected as shown in panel a) with the colors corresponding to the different components. The grey background area in panel corresponds to all auroral pixels. Some of the colored dots overlap.

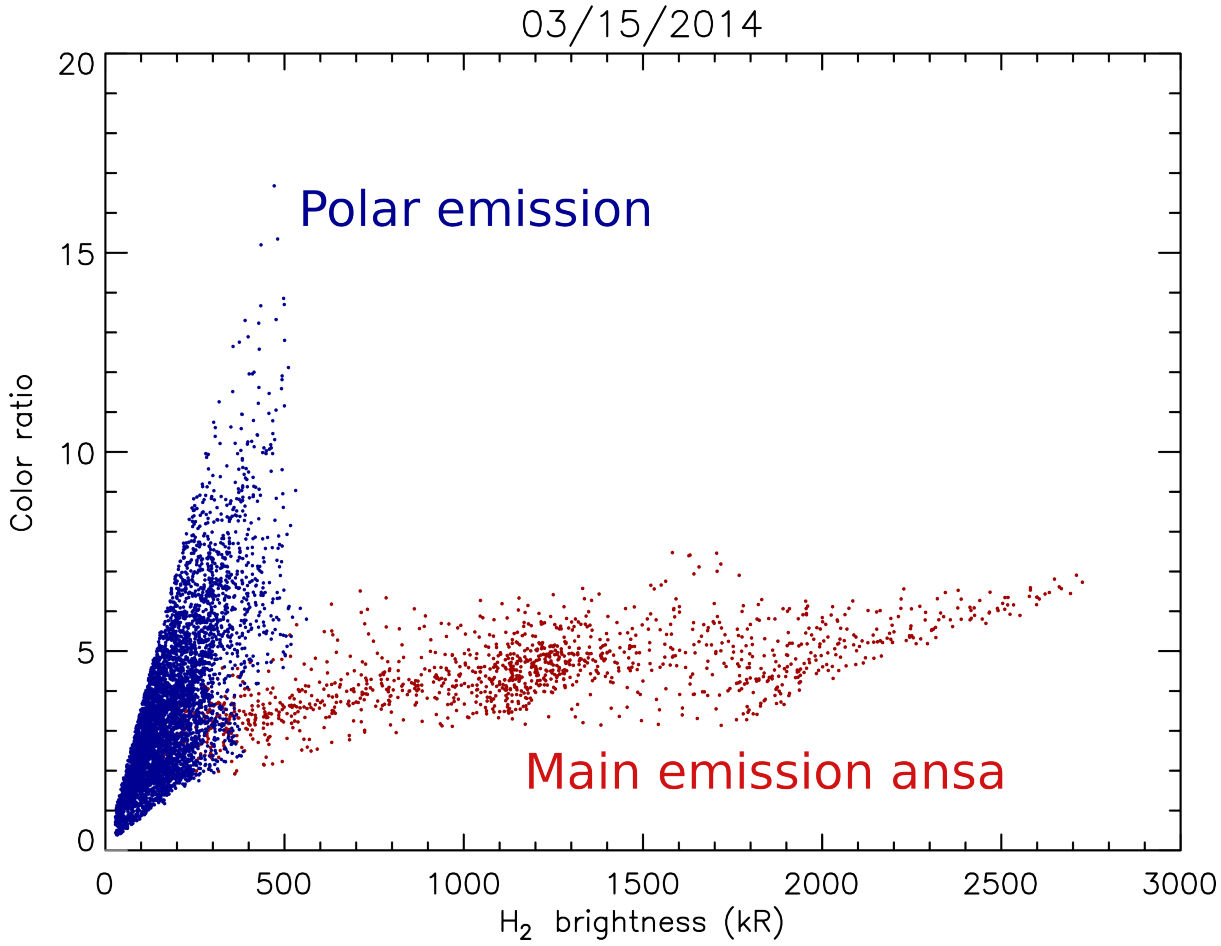

Figure 6: relationship between the FUV color ratio and the total H_2 auroral brightness measured on 15 March 2014 in the dusk ansa of the main emission (red dots) and polar flare (blue dots) regions.

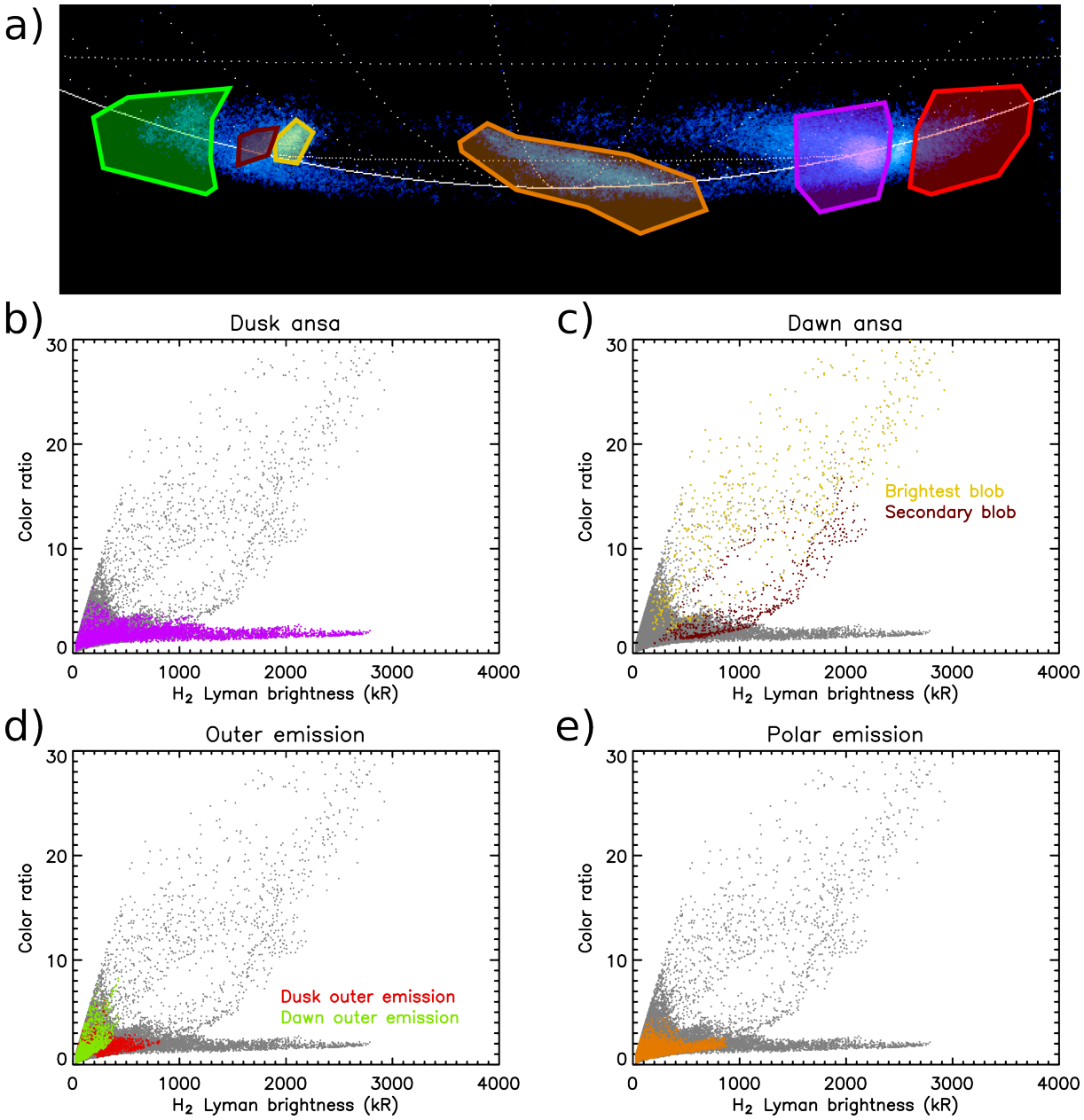

Figure 7: a) reconstructed image of 12 January 2014 divided into auroral components. The position of the planetary limb at the 1 bar level is shown by the white line. The white dotted lines show the 75° and 60° south parallels and the meridians at 10° intervals. Panels b) to e): observed relationship between the FUV color ratio and the total H_2 auroral brightness. Several auroral regions have been selected as shown in panel a) with the colors corresponding to the different components. The grey background area corresponds to all auroral pixels. Some of the colored dots overlap.